Preparation and crystallization of hollow α-Fe_2O_3 microspheres following the gas-bubble template method

L. de los Santos Valladares[1*], L. León Félix[2,3], S.M. Espinoza Suarez[2], A.G. Bustamante Dominguez[2], T. Mitrelias[1], S. Holmes[1], N.O Moreno[4], J. Albino Aguiar[5], C.H.W. Barnes[1]

[1] *Cavendish Laboratory, Department of Physics, University of Cambridge, J.J Thomson Av., Cambridge CB3 0HE, United Kingdom.*
[2] *Laboratorio de Cerámicos y Nanomateriales, Facultad de Ciencias Físicas, Universidad Nacional Mayor de San Marcos, Ap. Postal 14-0149, Lima, Peru.*
[3] *Laboratory of Magnetic Characterization, Instituto de Física, Universidade de Brasília, DF 70910-900, Brasilia, Brazil.*
[4] *Departamento de Física, Universidade Federal de Sergipe,* 49100-000, *Sao Cristóvao, Sergipe, Brazil.*
[5] *Laboratório de Supercondutividade e Materiais Avançados, Departamento de Física, Universidade Federal de Pernambuco 50670-901, Recife, Brazil.*

* Author to whom correspondence should be addressed, e-mails: ld301@cam.ac.uk and luisitodv@yahoo.es

Abstract In this work we report the formation of hollow α-Fe_2O_3 (hematite) microspheres by the gas-bubble template method. This technique is simple and it does not require hard templates, surfactants, special conditions of atmosphere or complex steps. After reacting $Fe(NO_3)_3.9H_2O$ and citric acid in water by sol-gel, the precursor was annealed in air at different temperatures between 180 and 600 ºC. Annealing at 550 and 600 ºC generates bubbles on the melt which crystallize and oxidizes to form hematite hollow spheres after condensation. The morphology and crystal evolution are studied by means of X-ray diffraction and scanning electron microscopy. We found that after annealing at 250-400 ºC, the sample consist of a mixture of magnetite, maghemite and hematite. Single hematite phase in the form of hollow microspheres is obtained after annealing at 500 and 600 ºC. The crystallization and crystal size of the hematite shells increase with annealing temperature. A possible mechanism for hollow sphere formation is presented.

Keywords: nanostructures; oxides; crystal growth; X-ray diffraction; magnetic materials.

1- Introduction

The production of hollow microspheres is of current interest due to their promising applications in photonic crystals, encapsulation, drug delivery, catalysis, chemical storage, light fillers and low dielectric constant materials [1-14]. A variety of hollow spheres such as carbide [15], Ni [16], TiO_2 [17], NiS [18], Bi_2Te_3 [19] and ZnO/SnO_2 [20] have been successfully fabricated. The most common techniques to produce hollow spheres are based on the use of core organic/inorganic hard templates such as monodispersed silica spheres [21-23], polymer latex colloids [11, 24], carbon spheres [25] and block copolymers [26, 27] or soft templates, such as emulsion droplets [28,29], surfactants vesicles [30] and liposome [31]. In general, the template technique involves four major steps (as represented in Fig. 1) [1]: (1) Preparation of the templates; (2) functionalization/modification of the templates surface to achieve favourable surface properties; (3) coating the templates with desired materials or their precursors; and (4) selective removal of the templates in appropriate solvents or calcination to obtain the hollow structures.

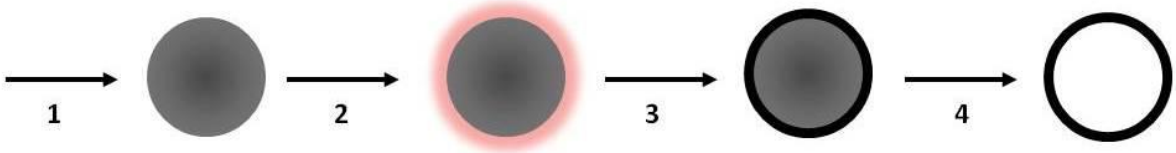

Fig. 1. Schematic representation of the process of hollow spheres by using templates. A typical procedure consists of (1) Preparation of the templates (2) functionalization/modification of their surface, (3) coating them and (4) removal or dissolution of the templates to obtain the hollow structures. (Adapted from Reference [1]).

The hard template technique is effective for controlling the morphology of the final product. Nevertheless, this technique requires tedious synthetic procedures such as a careful

selection of an affine template and a lot of care to prevent the collapse to affecting the quality of the shell during template removal. Some other drawbacks include limited sphere size, quality, purity, cost of production, and low temperature capability of the produced hollow spheres.

Recently different free-template approaches have been developed to produce hollow spheres. Some of these methods are based on Oswald ripening [32], simultaneous blowing and melting hidrogels [33-35], Kirkendall Effect [36-38], among others. However the average size of the hollow spheres produced by these methods are usually larger than 10 μm. Furthermore, it is difficult to obtain small microspheres having a narrow particle size distribution, and high purity metal oxide composition. Another less explored method for the production of hollow spheres is 'the gas-bubble template method'. This method involves the production of gas microbubbles during the chemical preparation of nanoparticles by using selected ligands. It is belived that the nanoparticles cover the surface and become hollow spheres after calcinations at high temperatures [39-46]. However the exact mechanism for the bubble nucleation and grow is unclear.

Hematite is the most stable iron oxide. It is *n*-type semiconductor (E_g=2.2 eV) under ambient conditions and it is easy to synthesize. Due to its magnetic properties, corrosion-resistance, low cost and low toxicity it is widely used in catalysis [47-50], environmental protection [51-57], sensors [58-61], magnetic storage materials [62] and clinic diagnosis and treatment [63]. To date, the preparation of a variety of hematite morphologies such as rhombohedra [64], particles [65-68], nanocubes [69, 70], rings [71], wires [72, 73], rods [74,75], fibbers [76], flakes [77], cages [78], airplane-like structures [79] and hierarchical structures [80-82] have been reported. Recently, some works have reported the production of

crystalline hematite hollow spheres through various methods. Some of the approaches are listed in Table 1. Note that most of the existing methods for obtaining the hematite hollow spheres involve templates, surfactants, toxic organic solvents, or complex steps. Among them, the hydrothermal/solvothermal method has some advantage over the rest due to its fast reaction time, effective control of particle shape, and low incorporation of impurities into the products. However, this technique requires of steel pressure vessels or autoclaves during preparation to apply high pressure and thus to achieve the formation of the hollow spheres [88-96]. In contrast, in this work we report the preparation of hematite hollow spheres by the gas-bubble template technique in which no high pressure or any special conditions of atmosphere are required. Here, the hollow hematite microspheres are formed by annealing sol-gel iron oxide precursor in air. We propose a mechanism for the hollow formation based on the condensation, crystallization and oxidation of bubbles shells at high temperatures. This method is reproducible, simple, cheap, environmental friendly and it allows good control of the size, crystallization and oxidation of the product.

Table 1. Some of the methods to produce hollow hematite microspheres reported in the literature. CTAB: cetyltrimethylammonium bromide. NM: Not mentioned.

Method	Diameter	Thickness of shells	Procedure	Reference
Polystyrene template	2.3 µm (average)	290 nm	Hydrothermal reaction between $FeSO_4$ and $KClO_3$ to obtain polystyrene/hematite composite shells.	[83]
Carbonaceous template	100-400 nm (outer)	20 nm	After stirring carbon templates with $Fe(NO_3)_3.9H_2O$ in ethanol at 35ºC, the gel was calcined at 250, 350 and 400 ºC.	[84]
Carbonaceous templates	1.2 µm (outer)	35-40 nm	Carbonaceous microspheres were coated with Fe^{3+} in ethanol following calcination	[85]
Carbonaceous templates	100-150 nm (outer)	< 20 nm	Carbon nanospheres were dispersed in $FeCl_3$ aqueous solution. After aging for 24 h it was heated at 450 ºC.	[86]
Electrospinning	500 nm (average)	60 nm	Polyvinylpyrrolidone and $Fe(NO_3)_3.9H_2O$ were reacted in	[87]

			ethanol and 18 kV was applied. It was calcined at 450-950 ºC for 2 h.	
Hydrothermal	2-5 µm (outer)	≈500 nm	$Fe(ClO_4)_3$ solution was reacted with sodium polyanethol sulphonate at 160 ºC in a Teflon-lined autoclave.	[88]
Hydrothermal	150-200 nm (outer)	10 nm	$FeCl_3 \cdot 7H_2O$ and NaH_2PO_4 were dissolved in H_2O and heated at 200 ºC in a Teflon-lined autoclave.	[89]
Hydrothermal	~ 1 µm (outer)	~ 300 nm	Hydrothermal process of $Fe_2(SO_4)_3$ and H_2O to obtain FeOOH hollow spheres followed by thermal annealing.	[90]
Hydrothermal	3-4 µm (average)	150 nm	CH_3COOH and $FeCl_3.6H_2O$ were mixed and heated at 160 ºC for 20 h.	[91]
Hydrothermal	150-200 nm (outer)	15-20 nm	After dissolving $K_4Fe(CN)_6$, CTAB, $(NH_4)_2S_2O_8$ and NaH_2PO_4 in H_2O, the solution was heated at 180 ºC for 8 h.	[92]
Hydrothermal	280 nm (outer)	60 nm	After mixing $K_3[Fe(CN)_6]$ and $(NH_4)_2HPO_4$ in water, it was heated at 220º for 24 h.	[93]
Polyoxometalate -assisted hydrothermal	600-700 nm (outer)	< 100 nm	After stirring $FeCl_3$ and $H_3PW_{12}O_{40}$ in H_2O, the solution was heated at 180 ºC for 8 h.	[94]
Surfactant-assited solvothermal	1.2 µm (average)	50 nm	After dissolving $FeSO_4.7H_2O$ and glucose in H_2O, and adding CTAB, the solution was heated at 120 ºC for 24 h and then at 140 ºC for 4 h.	[95]
Surfactant-assisted solvothermal	0.5 - 2 µm	100-500 nm	$FeCl_3.6H_2O$ was dissolved in ethanol in the presence of the surfactant CTAB and heated at 160 ºC for 24 h.	[96]
Sonochemical	12 nm (inner)	NM	Iron oxide carbon nanoparticles in iron pentacarbonyl with hexadecane were sonicated at 20 kHz and 20 ºC for 3 h. (The technique might be hazardous during autoignition)	[97]

2.- Experimental

Hollow hematite microspheres were produced by a modified gas-bubble template method following annealing in air an iron oxide precursor obtained by sol-gel [98]. For the precursor, 200 ml of colloidal ferric nitrate nine-hydrate ($Fe(NO_3)_3.9H_2O$) particles and mono hydrated citric acid ($C_6H_8O_7.H_2O$, 0.2M) were disolved in 800 ml of de-ionized. The solution was vigorously agitated in a magnetic stirrer at 350 rpm (70 ºC) for a period of 48 h to form $Fe(OH)_3$. The citric acid was used as ligand, to promote hydrolisis and to balance any difference of ions in the solution. A gel is formed by the hydrolisis of the ferric nitrate to iron oxohydrate FeOOH polymer [99].

The gel was then dried for two days at 40 ºC to evaporate the acid, water residuals and other possible impurities formed during hydrolysis. This sample precursor was then introduced in a tubular furnace (LENTON LTF-PTF Model 16/610) for annealing in air at different temperatures, from 180 to 600 ºC. The furnace was programmed to increase the temperature at 2 ±1 ºC/min, to remain constant for 12 h, and finally to cool down at a rate of 2 ± 0.5 ºC/min. This step has two purposes. First, to thermally oxidize the gel to obtain pure hematite; and secondly, to form bubble structures via boiling in air from which the hollow spheres are formed after quenching. Remarkably, the solution precursor, is stable in air and has a shelf life longer than two years. After reacting with water and following the same annealing process, similar hollow spheres can be obtained, confirming the reproducibility of the results.

The characterization of the sample was performed by X-ray diffraction (XRD). The data was collected from 20º to 65º (0.02º steps) using a powder universal diffractometer Bruker D8 Focus with Cu-K_α radiation (1.5406 Å). The diffractograms corresponding to the single hematite phase were refined using the Rietveld method and the peaks shape was modelled with a Pseudo-Voigt function (a combination of Gaussian and Lorentzian

functions). The average crystallite size for the single-phase hematite samples was estimated with the Scherrer equation [100]. During Rietveld refinement, R_{WP}/R_{exp} (the rate of the parameters *R*-weighted and *R*-expected) was used to observe the convergence of the cell parameters and to obtain a good fitting [101]. The shape of the hematite crystallite was modelled by using the program Vesta v.3.2.1 [102] and their strain were calculated with the Williamson-Hall method [103]. The morphological analysis was performed using a scanning electron microscope (SEM–XL30 SFEG). With the help of the Image-J software, several SEM images have been used to count $N \sim 1{,}000$ particles. Subsequently, particle size histograms have been mounted using the Sturges method [104, 105].

3 Results and discussion

Figure 2 shows the X-ray diffraction patterns of the samples after annealing at different temperatures from 180 to 600 ºC. Initially, after annealing at 180 ºC, the sample consists of an amorphous solid with no preferred reflections in the XRD. After annealing at 250 ºC, magnetite (Fe_3O_4) and maghemite (γ-Fe_2O_3) coexisting with a small amount of hematite (α-Fe_2O_3) were found. The first two phases were differentiated in the XRD by following the Kim's method [106], in which the (511) peak around 57º is deconvoluted into two peaks corresponding to magnetite (PDF2-No. 85-1436) and maghemite (PDF2-No. 04-0755) respectively; whereas the hematite was identified from its main reflection (104) at 33.16º. The variation of the annealing temperature from 250 to 400 ºC increases the presence of hematite (PDF2-No. 86-550) and its reflections (104), (110), (113), (024) and (300). Moreover, the amounts of hematite, magnetite and maghemite obtained by Rietveld refinement are: 11.83 % hematite, 54.57% magnetite and 33.60 maghemite (for the sample annealed at 250 ºC), and 43.57% hematite, 41.13% maghemite and 15.30% magnetite (for the sample annealed at 400 ºC). Increasing the annealing temperature to higher values, such as

500, 550 or 600 ºC, the total transformation of maghemite into hematite is obtained. Similar results have been reported by other authors [107, 108]. Note that the sharpness of the hematite peaks improves with annealing temperature meaning that the crystallization improves and the grain size increase. Eventually, after annealing the sample at 600 ºC, all Bragg reflections are consistent with the hematite phase, confirming the complete phase transition.

Hematite has a rhombohedrally centered hexagonal structure of corundum type (space group R-3C) with a close-packed oxygen lattice in which two-thirds of the octahedral sites are occupied by Fe(III) ions [109, 110]. The crystal parameters were obtained by Rietveld refinement, where R_{WP}/R_{EXP} (the R-weighted to R-expected ratio) was used to observe the convergence of the fitting parameter and to obtain a good fitting (See Fig. S1). The crystal parameters of the hematite are listed in Table 2, whereas the atomic positions for this phase are listed in Table 3. Some bonding lengths and bonding angles are listed in Table S1. Note that the crystallite size increases with annealing temperature while the residual strain decreases. In fact, these variations occur because the driving force increases with temperature making to overstep the equilibrium boundary to a more stable phase. The shape of the crystallite is described in more detail below.

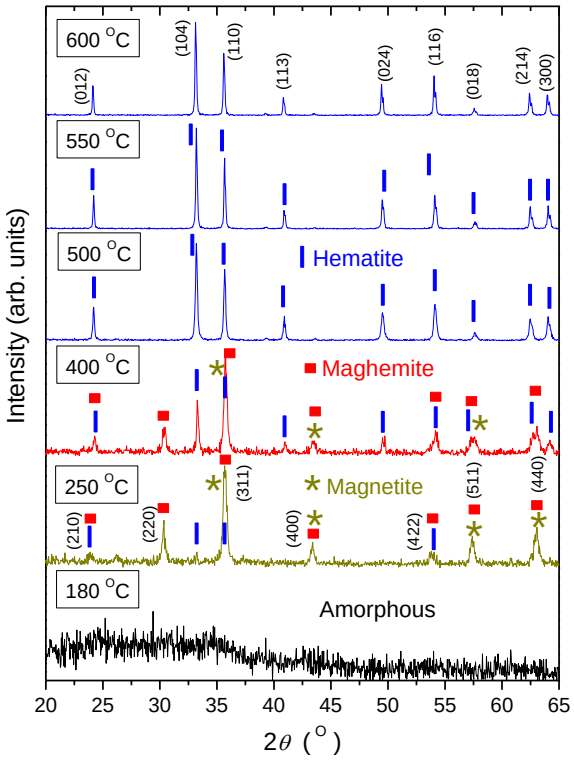

Fig. 2 X-ray diffraction patterns of the samples after annealing at different temperatures. After annealing at 180 ºC, the sample consists of an amorphous solid with no preferred reflections. After annealing at 250 ºC, magnetite and maghemite coexist with an small amount of hematite. Annealing at temperatures above 400 ºC increases the presence of hematite. Annealing at 500, 550 or 600 ºC results in the single-phase hematite.

Table 2: Crystallite size, lattice parameters and residual strains obtained by Rietveld refinements from XRD for the hematite phase.

Annealing Temperature (ºC)	$< D >$ **(nm)**	**Strain (%)**	***a*=*b* (Å)**	***c* (Å)**	R_{WP}/R_{Exp}
600	73.50	0.121	5.0338	13.7472	1.11
550	57.30	0.128	5.0338	13.7378	1.15
500	46.60	0.195	5.0339	13.7487	1.13
400	42.50	0.199	5.0372	13.7470	2.84
250	33.70	0.207	5.0372	13.7471	3.25

Table 3. Crystal parameters and atomic positions for the hematite phase obtained in this work. Crystal structure: trigonal, space group: R3c (*a*= 5.0340 Å, *c*= 13.7475 Å).

Atom	**Wyckoff**	**Valence**	**x**	**y**	**z**	**Occupancy**
Fe	*c*	+3	0	0	0.3552	1

O	*E*	-2	0.306	0	0.25	1

Figure 3 shows the scanning electron micrographs of the raw sample and after annealing at 550 and 600 ºC. Fig 3(a) shows the morphology of the sample obtained after sol-gel processing. The sample consists mainly of an formless mass of $Fe(OH)_x^{+(3-x)}$, H_2O and NO_3 [111]. Similar morphology was obtained for the samples annealed at temperatures below 500 ºC (not shown here). This in contrast to the hydrothermal method, in which intermediate solid cores or urchain-like seeds were observed after increasing the temperature [90-92]. In the present work the morphology of the sample continued un-shaped even after annealing at 500 ºC.

Fig. 3 (b) shows the morphology of the sample after annealing at 550 ºC, in which most of the material consists of micropheres with soft surfaces, coexisting with a few unshaped grains. The corresponding histogram (top right inset figure) gives a mean diameter of 889 ± 20 nm. The top left inset figure shows a broken sphere revealing its internal cavity. The broken sphere has an external diameter of around 1.45 µm and shell thickness of around 200 nm. Fig. 3 (c) shows the sample after annealing at 600 ºC. The mean size of the spheres has increased to around 1.60 µm as noted from its respective histogram (top right inset figure). The top left inset figure shows a broken sphere with an external diameter of 2 µm and shell thickness of less than 100 nm. The difference in diameter and shell thickness than in the previous case suggests that, as the size of the spheres grows, the shells become thinner.

Fig. 3(d) shows one sphere with diameter 1.85 µm obtained after annealing at 600 ºC. Note that the surface is not completely soft and it presents a rough surface suggesting that it is composed of different grains. A model of the crystallite shape of this sample is provided in the top right inset figure. Note that the shape of the grains conforming the shell are slightly

similar to the modelled crystallite orientated along the {104} and {110} family of planes. However, since the crystallite size of this sample is 73.5 nm (see Table 2), each grain in the shell should contain between 1 - 3 crystallites. Note that by increasing the annealing temperature from 550 to 600 ºC the crystallite size increases and the shell thickness decreases. In this way, the calculated number of crystallites forming the shell of the sample annealed at 550 ºC is around 3.1×10^3, whereas that for the sample annealed at 600 ºC is around 2.6×10^3. This slightly difference number of crystallites indicates that the spheres growth is quasi-isotropic.

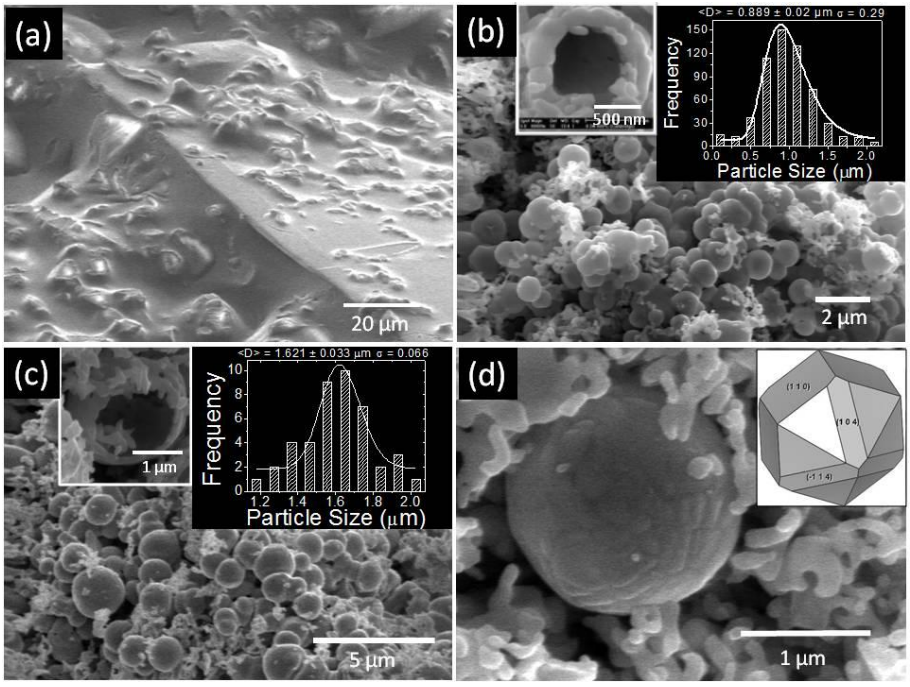

Fig. 3. Scanning electron microscope micrograph of the raw sample and after annealing at 550 and 600 ºC. a) Sample obtained after sol-gel processing (raw). b) Sample after annealed at 550 ºC. Top right inset: histogram giving a mean diameter of 889 ± 20 nm. Top left inset: A broken sphere revealing its internal cavity. c) Sample after annealing at 600 ºC. Top right inset: Histogram giving a mean diameter of 1.60 µm. Top left inset: A broken sphere revealing its internal cavity. d) An individual sphere obtained after annealing at 600 ºC. Top

right inset: A model of the crystallite shape of the hematite orientated along the {104} and {110} family planes.

In order to understand better the bubble formation we have exposed the raw iron oxide precursor to an electron beam generated in a SEM. Figure 4 shows the SEM image of the raw sample obtained by secondary electrons accelerated at 5 kV at consecutive times. The inset figures show the topography profile on the areas pointed by the arrows. Fig. 4 (a) shows an image taken at an initial time set as 0 s when the electron beam starts heating the sample. Fig. 4 (b) shows the same area scan after 5 s of electron beam irradiation. Remarkably, bloating areas form in different parts over the surface. The arrow points a clear formed bubble caused by the heated sample due to electron beam incidence. The bubble should consist of diffusive gas tending to escape from the sample and remained trapped due to surface tension. Figure 4 (c) shows the morphology of the same area after 10 s of electron beam irradiation. The bubble pointed by the arrow has exploded. It is difficult to calculate the internal pressure of the gas before exposion because it depends not only on the diameter but also on surface tension of the bubble. However, since the internal pressure of a bubble increase on decreasing its diameter [112], the explosion observed in the figure should be caused by increment on the outgass species promoted by heating due to the long beam exposure. Similar works about bubble formation in other materials report that the internal pressure varies over a wide range (from 10 [113] to 300 × 10^6 Pa [114]) and it also depends on the type of and gas. Thus, this technique is suitable for the encapsulation of pure or preselected combination of gases.

The mechanism for the formation of the hollow spheres in this work might be as follow:

1st- Initially, dissolution of the reagents occurs:

$$Fe(NO_3).9H_2O_{(s)} \xrightarrow{H_2O} Fe^{3+} + NO_3^-{}_{(aq)} \quad (1)$$

$$H_3C_6H_5O_7.H_2O_{(s)} \xrightarrow{H_2O} H_3C_6H_5O_{7\,(aq)} \quad (2)$$

Reaction between the dissolved reagents occurs via hydrolyzation of iron and nitrate. The nitrate (NO_3^-) solubilize in water while the Fe^{3+} ions react progressively with water and the decomposed products of the citric acid to form an hydrated iron-citrate gel which after drying (equation 6) an amorphous compound of Fe, C, H and O ions is formed, as observed in Fig. 3 (a) and Fig. (4).

$$Fe(OH)_{3\,(gel)} + H_3C_6H_5O_{7\,(aq)} \xrightarrow{\text{drying}} FeC_6H_5O_{7\,(s)} + 3H_2O_{(g)} \quad (3)$$

2nd- During annealing, the latest product reacts with air to form magnetite, maghemite or hematite depending on the temperature (as detected by XRD in Fig. 2). In the case of hematite:

$$FeC_6H_5O_{7\,(s)} + air \xrightarrow{\Delta} Fe_2O_{3\,(S)} + H_2O_{(v)} + CO_{2\,(g)} \quad (4)$$

the reaction occurs with simultaneous melting, vaporization and degassing of the precursor components. In addition to H_2O and CO_2, N_2, NO and O_2 might also become volatile due to the decomposition of NO_3 [111].

3rd- At high annealing temperatures, such as 550 and 600 ºC, the melt superheats and decompresses. Decompression exerts a major control on the physical state of the melt. This change in pressure influences the density and solubility of the gaseous components. A chaotic internal diffusion occurs forming a vesicular texture in which the superheated gases take place. These cavities act as heterogeneous nucleation centres for single crystal growth or polycrystalline aggregation [115].

4th.- The exact processes that control the nucleation and growth of the gas bubbles are complex and highly nonlinear [116]. It is assumed that a bubble nucleates when superheated liquid grows sufficiently to cause the vapour/gas trapped within the cavity to overcome the surface tension force and should grow following the theory of Hsu [117].

5th- Once a bubble nucleates, it grows through: (i) mechanical expansion due to compressibility of the gas phase and (ii) simultaneous diffusion from the superheated melt to adjacent bubbles and evaporation of the liquid in the surface bubble [118]. The transport of water to the bubbles' interface has not been much investigated, but the growth rate of a bubble was parameterized following the relation [119]:

$$\frac{R(t)}{R_i} = e^{\frac{\tau^2 t_{dec}}{2t_{vis}}} \quad (5)$$

where $R(t)$ is the radius of the bubble at a particular time, R_i is the radius previous to decompression, t_{vis} is the timescale for viscous relaxation, t_{dec} is the timescale for decompression and $\tau = \left| {}^{dp}/_{dt} \right| t$ in which p is the pressure.

6th- Whereas, the viscosity of the surrounding melt opposes a resistance to bubbles growth. The surface tension acts on the bubbles shrinking the surface and forces them back to the melt. Thus, there is a competition between the buoyancy and surface tension, which is mediated by the temperature. Approaching the surface, the external pressure decreases and the bubbles evolve in the liquid.

7th.- Thus, the microbubbles act as soft templates over which crystallites aggregate and grow. Eventually, the crystallization, condensation and oxidation of the shells is controlled by the

heat treatments, thus forming the hollow spheres. A similar mechanism has been also proposed by other authors [120].

The parameters that can be adjusted for controlling the size, shell thickness, crystallization, oxidation and quality of the bubbles are: the annealing temperature, the increase/decrease ratio of temperature, the annealing time, the solvent and the concentration of the reactants (and hence viscosity of the precursor). Among them, the annealing temperature has a high influence in the size, shell thickness and crystallization of the product. In this sense, it is expected that for higher annealing temperatures than 600 ºC the percentage of broken bubbles in the final product increases. The annealing atmosphere (which is air in this work and can be changed easily in the tubular furnace) is an important proven controlling parameter for solid state reactions and have great influence on the reaction as well as the morphology of the product magnetic iron oxides. Moreover, the concentration of the reactants also plays an important role. The concentration of the citric acid plays an important role as well. We observed that citric acid with concentrations lower than 0.1 M (data not shown here) do not produce enough gas to form the microbubbles. The concentration of citric acid used in the present work was 0.2 M resulting in high quality hollow spheres. Whereas, it is expected that using higher molarities might result in thicker shells and smaller diameter for the bubbles [119]. In such a case, the diameter of the hollow spheres can be increased by raising the annealing temperature. Furthermore, the slow heating/quenching rate (2 ºC/min) also assist in yielding intact, dense, and stronger spheres by allowing the nascent, individual bubbles to crystallize completely as separated particles.

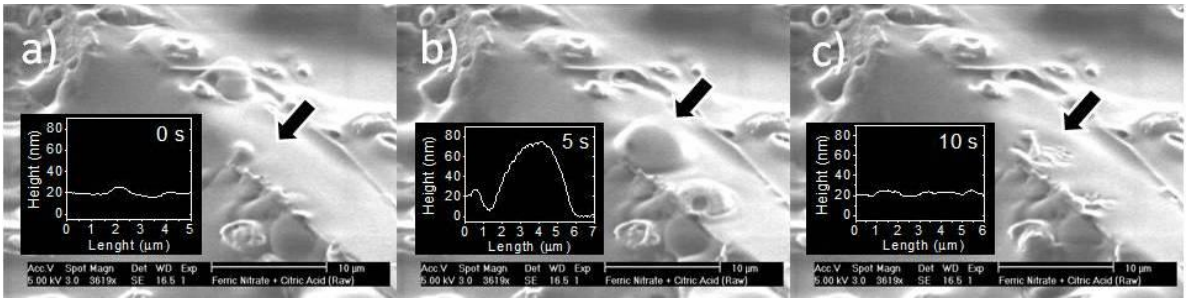

Fig. 4. SEM micrographs of the raw sample obtained by secondary electrons accelerated at 5 kV at consecutive times: a) 0 s, b) 5 s and c) 10 s. The arrows point areas in which a clear bubble is formed. The inset figure shows the corresponding topography profile over the area pointed by the arrows.

The technique presented in this work is environmental friendly since: i) The reagent ingredients (citric acid, nitrate, water, etc) are not toxic, ii) no toxic gases are produced during reaction (see equations (1) to (4)) and iii) the resulting product (hematite) is not toxic either. Thus, due to the simplicity of the technique presented here for the preparation of hematite hollow spheres, we feel that the results of this work could have important application in the emerging fields of targeted treatment, such as targeted cancer treatment. Our group has studied the synthesis, characterization and functionalization of different magnetic nanocomplexes together with some clinical tests on animals [121-128]. The hollow spheres presented here could be used as drug delivery vehicles and potentially this approach could result in replacing chemotherapy with the well known very adverse and serious side effects, with a targeted delivery of the anticancer drug only to the areas of the tumors, for example by direct injection to the solid tumors. Moreover, hyperthermia in which the temperature around solid tumors is raised is also a very promising approach in cancer treatment in which we have been working. Since the ferromagnetic behavior of the hollow

hematite spheres is sensed better to higher temperatures than RT, then they can be very suitable candidates as agents of targeted hyperthermia.

4 Conclusions

Hollow hematite microspheres were prepared by the gas-bubble template method. Boiling at high temperatures promotes bubble formation on which crystallites agglomerate, crystallize and oxidize to the hematite phase leading in the formation of hollow microspheres. The size and crystallization of the hematite hollow spheres increases with annealing temperature. After annealing at 550 ºC, hollow spheres with mean diameter of 0.889 μm are obtained, whereas after annealing at 600 ºC, hollow spheres of 1.6 μm are obtained. The increase in diameter is accompanied with a slight decrease of the thickness of the shells suggesting that the growth of the hollow spheres depends on the bubble growth.

Acknowledgements. This work was supported by the Engineering and Physical Science Research Council (EPSRC No. EP/J003638/1). The work in Peru has been supported by CONCYTEC. The work in Brazil was supported by CNPq (307552/2012-8), CAPES (PNPD-230.007518/2011-11) and FACEPE (APQ-0589-1.05/08).

References

[1] X.W. Lou, L.A. Archer, Z.C. Yang, Adv. Mater. 20 (2008) 3987-4019.
[2] F. Caruso, Top. Curr. Chem. 227 (2003) 145.
[3] F. Caruso, Adv. Mater. 13 (2001) 11.
[4] W. Schärtl, Adv. Mater. 12 (2000) 1899.
[5] R. Pelton, Adv. Colloid Interface Sci. 85 (2000) 1.
[6] D. Gan, L. Lyon, J. Am. Chem. Soc. 123 (2003) 7511.
[7] C. Jones, L. Lyon, Macromolecules 36 (2003) 1988.
[8] F. Caruso, R.A. Caruso, H. Möhwald, Science 282 (1998) 1111.
[9] F. Caruso, Chem. Eur. J. 6 (2000) 413.
[10] Z. Zhong, Y. Yin, B. Gates, Y. Yia, Adv. Mater. 12 (2000) 206.
[11] C.E. Fowler, D. Khushalani, S. Mann, J. Mater. Chem. 11 (2001) 1968.
[12] W.R. Zhao, H.R. Chen, Y.S. Li, L. Li, M.D. Lang, J.L. Shi, Adv. Funct. Mater. 16 (2006) 2243.
[13] J. Bertling, J. Blömer, R. Kummel, Chem. Eng. Technol. 27 (2004) 829.

[14] L.F. Xiao, Y.Q. Zhao, J. Yin, L.Z. Zhang, Chem. Eur. J. 15 (2009) 9442.
[15] C. Li, X. Yang, B. Yang, Y. Yan, Y.T. Qian, Eur. J. Inorg. Chem. 2003 (2003) 3534.
[16] J. Bao, Y. Liang, Z. Xu, L. Si, Adv. Mater. 15 (2003) 1832.
[17] F. Caruso, X. Shi, R.A. Caruso, A. Susha, Adv. Mater. 13 (2001) 740.
[18] Y. Hu, J. Chen, W. Chen, X. Lin, X. Li, Adv. Mater. 15 (2003) 726.
[19] Y. Jiang, Y.J. Zhu, L.D. Chen, Chem. Lett. 36 (2007) 382.
[20] W.W. Wang, Y.J. Zhu, L.X. Yang, Adv. Funct. Mater. 17 (2007) 59.
[21] N. Du, H. Zhang, J. Chen, J. Sun, B. Chen, D. Yang, J. Phys. Chem. B 112 (2008) 14836.
[22] G.X. Liu, G.Y. Hong, J. Solid State Chem. 178 (2005) 1647.
[23] N.A. Dhas, K.S. Suslick, J. Am. Chem. Soc. 127 (2005) 2368-2369.
[24] R.A. Caruso, A. Susha, F. Caruso, Chem. Mater. 13 (2001) 400.
[25] W. Shen, Y. Zhu, X. Dong, J. Gu, J. Shi, Chem. Lett. 34 (2005) 840.
[26] L. Qi, J. Li, J. Ma, Adv. Mater. 14 (2002) 300-303.
[27] T. Liu, Y. Xie, B. Chu, Langmuir 16 (2000) 9015-9022.
[28] T. Chen, P.J. Colver, S.A.F. Bon, Adv. Mater. 19 (2007) 2286.
[29] C. Zimmermann, C. Feldmann, M. Wanner, D. Gerthsen, Small 3 (2007) 1347.
[30] D.B. Zhang, L.M. Qi, J.M. Ma, H.M. Cheng, Adv. Mater. 14 (2002) 1499.
[31] H.T. Schmidt, A.E. Ostafin, Adv. Mater. 14 (2002) 532-535.
[32] X.W. Lou, Y. Wang, C. Yuan, J.Y. Lee, L.A. Archer, Adv. Mater. 18 (2006) 2325.
[33] W.R. Beck, D.L. O' Brien, U.S. Patent No. 3, 365, 315 (23 Jan. 1968).
[34] P.A. Howell, U.S. Patent No. 4,391, 646 (5 Jul. 1983).
[35] H.J. Marshall, U.S. Patent No. 4, 767, 726 (30 Aug. 1988).
[36] H.J. Fan, U. Gösele, M. Zacharias, Small 3 (2007) 1660-1671.
[37] Y.D. Yin, R.M. Rioux, C.K. Erdonmez, S. Hughes, G.A. Somorjai, A.P. Alivisatos, Science 304 (2004) 711.
[38] F. Aldinger, Acta Metallurgica, 22 (1974) 923-928.
[39] J.R. Rodríguez, A. Sevilla, C.M. Bazán, J.M. Gordillo, Annu. Rev. Fluid Mech. 47 (2015) 405-429.
[40] Y. Fang, G.Z. Xiao, J. Xin, W.H. Yao, G. Ning, Chin. Phys. B 22 (2013) 104301.
[41] C.Z. Wu, Y. Xie, L.Y. Lei, S.Q. Hu, C.Z. OuYang, Adv. Mater. 18 (2006) 1727.
[42] X.X. Li, Y.J. Xiong, Z.Q. Li, Y. Xie, Inorg. Chem. 45 (2006) 3493.
[43] L. Guo, F. Liang, X.G. Wen, S.H. Yang, L. He, W.Z. Zheng, C.P. Chen, Q.P. Zhong, Adv. Funct. Mater. 17 (2007) 425.
[44] Y.S. Han, G. Hadiko, M. Fuji, M. Takahashi, Chem. Lett. 34 (2005) 152.
[45] C.L. Jiang, W.Q. Zhang, G.F. Zou, W.C. Yu, Y.T. Qian, Nanotechnology 16 (2005) 551.
[46] Q. Peng, Y.J. Dong, Y.D. Li, Angew. Chem., Int. Ed. 42 (2003) 3027.
[47] J.L. Zhang, Y. Wang, H. Ji, Y.G. Wei, N.Z. Wu, B.J. Zuo, Q.L. Wang, J. Catal. 229 (2005) 114.
[48] O. Shekhah, W. Ranke, A. Schule, G. Kolios, R. Schlogl, Angew. Chem. Int. Ed. 42 (2003) 5760.
[49] A.S.C. Brown, J.S.J. Hargreaves, B. Rijniersce, Catal. Lett. 53 (1998) 7.
[50] B.C. Faust, M.R. Hoffmann, D.W. Bahnemann, J. Phys. Chem. 93 (1989) 6371.
[51] P. Li, D.E. Miser, S. Rabiei, R.T. Yadav, M.R. Hajaligo, Appl. Catal. B 43 (2003) 151.
[52] L.C.A. Oliveira, D.I. Petkowicz, A. Smaniotto, S.B.C. Pergher, Water Res. 38 (2004) 3699.
[53] C.H. Lai, C.Y. Chen, Chemosphere 44 (2001) 1177.
[54] M.S. Onyango, Y. Kojima, H. Matsuda, A. Ochieng, J. Chem. Eng. Jpn. 36 (2003) 1516.
[55] R.C. Wu, J.H. Qu, Y.S. Chen, Water Res. 39 (2005) 630.
[56] R.C. Wu, H.H. Qu, H. He, Y.B. Yu, Appl. Catal. B 48 (2004) 49.

[57] F. Herrera, A. Lopez, G. Mascolo, E. Albers, J. Kiwi, Appl. Catal. B 29 (2001) 147.
[58] J. Chen, L. Xu, W. Li, X. Gou, Adv. Mater. 17 (2005) 58.
[59] C.Z. Wu, P. Yin, X. Zhu, C.Z. OuYang, Y. Xie, J. Phys. Chem. B 110 (2006) 110.
[60] X.L. Gou, G.X. Wang, J. Park, H. Liu, J. Yang, Nanotechnology 19 (2008) 125605.
[61] J.S. Han, T. Bredow, D.E. Davey, A.B. Yu, D.E. Mulcahy, Sens. Actuators B 75 (2001) 18.
[62] H. Zeng, J. Li, J.P. Liu, Z.L. Wang, S.H. Sun, Nature 420 (2002) 95.
[63] A. Jordan, R. Scholz, K. Maier-Hauff, M. Johannsen, P. Wust, J. Nadobny, H. Schirra, H. Schmidt, S. Deger, S. Loening, W. Lanksch, R. Felix, J. Magn. Magn. Mater. 225 (2001) 118.
[64] T.J. Park, S.S. Wong, Chem. Mater. 18 (2006) 5289.
[65] Y.Y. Zhang, Q.J. Zheng, J. Phys. Chem. B 110 (2006) 3093.
[66] C.Q. Hu, Z.H. Gao, X.R. Yang, Mater. Chem. Phys. 104 (2007) 429.
[67] S. Komarneni, R. Roy, Q.H. Li, Mater. Res. Bull. 27 (1992) 1393.
[68] H. Katsuki, S.J. Komarneni, J. Am. Ceram. Soc. 84 (2001) 2313.
[69] S.B. Wang, Y.L. Min, S.H. Yu, J. Phys. Chem. C 111 (2007) 3551.
[70] B. Hou, Y. Wu, L. Wu, Y. Shi, K. Zou, H. Gai, Mater. Lett. 60 (2006) 3188-3191.
[71] X.L. Hu, J.C. Yu, J.M. Gong, Q. Li, G.S. Li, Adv. Mater. 19 (2007) 2324.
[72] Y.L. Chueh, M.W. Lai, J.Q. Liang, L.J. Chou, Z.L. Wang, Adv. Funct. Mater. 16 (2006) 2243.
[73] X.G. Wen, S.H. Wang, Y. Ding, Z.L. Wang, S.H. Yang, J. Phys. Chem. B 109 (2005) 215-220.
[74] J.J. Wu, Y.L. Lee, H.H. Chiang, D.K.P. Wong, J. Phys. Chem. B 110 (2006) 18108.
[75] L. Liu, H.Z. Kou, W.L. Mo, H.J. Liu, Y.Q. Wang, J. Phys. Chem. B 110 (2006) 15218-15223.
[76] C.R. Gong, D.R. Chen, X.L. Jiao, Q.L. Wang, J. Mater. Chem. 12 (2002) 1844.
[77] M.V. Reddy, T. Yu, C.H. Sow, Z.X. Shen, C.T. Lim, G.V.S. Rao, B.V.R. Chowdari, Adv. Funct. Mater. 17 (2007) 2792.
[78] D.B. Wang, C.X. Song, G.H. Gu, Z.S. Hu, Mater. Lett. 59 (2005) 782.
[79] S.Z. Li, H. Zhang, J.B. Wu, X.Y. Ma, S.R. Yang, Cryst. Growth Des. 6 (2006) 351-353.
[80] S.W Cao, Y.J. Zhu, J. Phy. Chem. C 112 (2008) 6253-6257.
[81] C. Jia, Y. Cheng, F. Bao, D.Q. Chen, Y.S. Wang, J. Cryst. Growth 294 (2006) 353-357.
[82] X.L. Hu, J.C. Yu, J.M. Gong, J. Phys. Chem. C 111 (2007) 11180.
[83] Y. Zhang, Y. Chu, L. Dong, Nanotechnology 18 (2007) 435608.
[84] D. Jagadeesan, U. Mansoori, P. Mandal, A. Sundaresan, M. Eswaramorthy, Angew. Chem. Int. Ed. 47 (2008) 7685-7688.
[85] S. Xu, C.M. Hessel, H. Ren, R. Yu, Q. Jin, M. Yang, H. Zhao, D. Wang, Energy Environ. Sci. 7 (2014) 632-637.
[86] L. Sun, M. Cao, C. Hu, Solid. State Sci. 12 (2010) 2020-2023.
[87] L. Wang, X. Lu, C. Han, R. Lu, S. Yang, X. Song, CrystEngComm 16 (2014) 10618-10623.
[88] I. Opačak, M. Ristić, S. Musić, Mater. Lett. 64 (2010) 2555-2558.
[89] H.J. Song, N. Li, X.Q. Shen, Appl. Phys. A 102 (2011) 559-563.
[90] P. Sun, Z. Zhu, P. Zhao, X. Liang, Y. Sun, F. Liu, G. Lu, Cryst. Eng. Comm. 14 (2012) 8335-8337.
[91] Q. Dong, N. Kumada, Y. Yonesaki, T. Takei, N. Kinomura, D. Wang, J. Mater. Sci. 45 (2010) 5685-5691.
[92] L. Li, Y. Chu, Y. Liu, L. Dong, J. Phys. Chem. C 111 (2007) 2123-2127.
[93] J. Ma, K. Chen, Phys. Status Solidi RRL 6 (2012) 324-326.

[94] B.D. Mao, Z.H. Kang, E.B. Wang, C.G. Tian, Z.M. Zhang, C.L. Wang, Y.L. Song, M.Y. Li, J. Solid State Chem. 180 (2007) 489-495.
[95] S. Ni, S. Lin, Q. Pan, F. Yang, K. Huang, X. Wang, D. He, J. Alloys Compd. 478 (2009) 876-879.
[96] S. Lian, E. Wang, L. Gao, D. Wu, Y. Song, L. Xu, Mater. Res. Bull. 41 (2006) 1192-1198.
[97] J.H. Bang, K.S. Suslick, J. Am. Chem. Soc. 129 (2007) 2242-2243.
[98] L. León, A. Bustamante, A. Osorio, G.S. Loarte, L. de los Santos Valladares, C.H.W. Barnes, Y. Majima, Hyperfine Interact. 202 (2011) 131-137.
[99] D. Jagadeesan, U. Mansoori, P. Mandal, A. Sundaresan, M. Eswaramoorthy, Angew. Chem. Int. Ed. 47 (2008) 7685-7688.
[100] Bernard Dennis Cullity, Elements of X-ray Diffraction, third ed., Prentice-Hall, Prentice-Hall International, Upper Saddle River, NJ, London, 2000.
[101] H. M. Rietveld, J. Appl. Cryst, 2 (1969) 65.
[102] K. Momma, F. Izumi, J. Appl. Crystallogr. 44 (2011) 1272-1276.
[103] G. K. Williamson and W. H. Hall, Acta Metall, 1 (1953) 22.
[104] Aragón, F.H., de Souza, P.E.N., Coaquira, J.A.H., Hidalgo, P., Gouvêa, D.: Physica B 407 (2012) 2601.
[105] L. León-Félix, J. Chaker, M. Parise, J.A.H. Coaquira, L. De Los Santos Valladares, A. Bustamante, V.K. Garg, A.C. Oliveira, P.C. Moris, Hyperfine Interact. 224 (2014) 179-188.
[106] W. Kim, C.Y. Suh, S.W. Cho, K.M. Roh, H. Kwon, K. Song, I.J. Shon, Talanta 94 (2012) 348-352.
[107] J. Zhang, L.X. Rong, Y. Liu, B.Z. Dong, Mat. Sci. Eng. A351 (2003) 224–227.
[108] K. Haneda, A.H. Morrish, J. Physique, Sup. 4, 38 (1977) C1-321–323..
[109] R. Zboril, M. Mashlan, D. Petridis, Chem. Mater. 14 (2002) 969.
[110] X. Wang, X.Y. Chen, X.C. Ma, H.G. Zheng, M.R. Ji, Z. Zhang, Chem. Phys. Lett. 384 (2004) 391.
[111] Q. Dong, D. Wang, J. Yao, N. Kumada, N. Kinomura, T. Takei, Y. Yonesaki, Q. Cai, J. Ceram. Soc. Jpn 117 (2009) 245-248.
[112] R. Parmar, S.K. Majumder, Chem. Eng. Process.: Process Intensification 64 (2013) 79-97.
[113] K.H. Moh, Mat. Res. Soc. Symp. Proc. 372 (1995) 15-23.
[114] L. De Los Santos Valladares, A. Bustamante Domínguez, J. Llandro, S. Holmes, O. Avalos Quispe, R. Langford, J. Albino Aguiar, C.H.W. Barnes, Appl. Surf. Sci. 316 (2014) 15-21.
[115] X. Chen, Z. Zhang, X. Li, C. Shi, Chem. Phys. Lett. 422 (2006) 294-298.
[116] J. Kim, Int. J. Multiph. Flows 35 (2009) 1067-1076.
[117] Y.Y. Hsu, J. Heat Transfer. 84 (1962) 207-213.
[118] J. Verhoogen, Am. J. Sci. 249 (1951) 729-739.
[119] C. Huber, Y. Su, C.T. Nguyen, A. Parmigiani, H.M. Gonnermann, J. Dufek, J. Geophys. Res. Solid Earth 119 (2014) 216-239.
[120] Z. Wu, K. Yu, S. Zhang, Y. Xie, J. Phys. Chem. C 112 (2008) 11307-11313.
[121] K.N. Vyas, D.M. Love, A. Ionescu, J. Llandro, P. Kollu, T. Mitrelias, S. Holmes, C.H.W. Barnes, Biosensors 5 (2015) 172-186.
[122] V.A.J. Silva, P.L. Andrade, A. Bustamante Domínguez, L. De Los Santos Valladares, M.S. Mejia, I.A. Souza, K.P.S. Cavalcanti, M.P.C. Silva, J. Albino Aguiar, Hyperf. Interact. 224 (2014) 227-238.
[123] V. Orel, T. Mitrelias, M. Tselepi, T. Golovko, O. Dynnyk, N. Nikolov, A. Romanov, A. Rykhalskiy, C.H.W. Barnes, O. Yaroshenko, I. Orel, D. Supruniuk, I. Schepotin, J. Nanopharmaceutics and Drug Delivery 2 (2014) 1-11.

[124] P.L. Andrade, V.A.J. Silva, J.C. Maciel, M. Mejía, N.O. Moreno, L. de los Santos Valladares, A. Bustamante, S.M.B. Pereira, M.P.C. Silva, J. Albino Aguiar, Hyperf. Interact. 224 (2014) 217-225.
[125] V.E. Orel, T. Mitrelias, M. Tselepi, E.I. Kruchkov, A.Y. Rykhalskiy, A.V. Romanov, T.S. Golovko, C.H.W. Barnes, I.B. Shchepotin, IFMBE Proceedings 51 (2015) 903-906.
[126] V.A. Silva, P.L. Andrade, M.P.C. Silva, A. Bustamante Domínguez, L. De Los Santos Valladares, J. Albino Aguiar, J. Magn. Magn. Mater. 343 (2013) 138 - 143.
[127] V. Orel, A. Shevchenko, A. Romanov, M. Tselepi, T. Mitrelias, C.H.W. Barnes, A. Burlaka, S. Lukin, I. Shchepotin, Nanomed: Nanotech. Biol. Med. 11 (2015) 47-55.
[128] L. De Los Santos Valladares, J. Llandro, D. Lee, T. Mitrelias, J.J. Palfreyman, T.J. Hayward, J. Cooper, J.A.C. Bland, C.H.W. Barnes, J. Arroyo Cuyubamba, M. Lees**,** J. Magn. Magn. Mater. 321 (2009) 2129-2134.